# Bioprinting and regeneration of auricular cartilage using a bioactive bioink based on microporous photocrosslinkable acellular cartilage matrix

Litao Jia [a,1], Yujie Hua [b,1], Jinshi Zeng [a], Wenshuai Liu [a], Di Wang [a], Guangdong Zhou [b,c,***], Xia Liu [a,**], Haiyue Jiang [a,*]

[a] *Research Center of Plastic Surgery Hospital, Chinese Academy of Medical Sciences and Peking Union Medical College, Beijing, 100144, PR China*
[b] *Department of Plastic and Reconstructive Surgery, Shanghai Ninth People's Hospital, Shanghai Key Laboratory of Tissue Engineering, Shanghai Jiao Tong University School of Medicine, Shanghai, 200011, PR China*
[c] *Research Institute of Plastic Surgery, Weifang Medical University, Weifang, 261042, PR China*

## ARTICLE INFO

## ABSTRACT

Tissue engineering provides a promising strategy for auricular reconstruction. Although the first international clinical breakthrough of tissue-engineered auricular reconstruction has been realized based on polymer scaffolds, this approach has not been recognized as a clinically available treatment because of its unsatisfactory clinical efficacy. This is mainly since reconstruction constructs easily cause inflammation and deformation. In this study, we present a novel strategy for the development of biological auricle equivalents with precise shapes, low immunogenicity, and excellent mechanics using auricular chondrocytes and a bioactive bioink based on biomimetic microporous methacrylate-modified acellular cartilage matrix (ACMMA) with the assistance of gelatin methacrylate (GelMA), poly(ethylene oxide) (PEO), and polycaprolactone (PCL) by integrating multi-nozzle bioprinting technology. Photocrosslinkable ACMMA is used to emulate the intricacy of the cartilage-specific microenvironment for active cellular behavior, while GelMA, PEO, and PCL are used to balance printability and physical properties for precise structural stability, form the microporous structure for unhindered nutrient exchange, and provide mechanical support for higher shape fidelity, respectively. Finally, mature auricular cartilage-like tissues with high morphological fidelity, excellent elasticity, abundant cartilage lacunae, and cartilage-specific ECM deposition are successfully regenerated *in vivo*, which provides new opportunities and novel strategies for the fabrication and regeneration of patient-specific auricular cartilage.

## 1. Introduction

Microtia is one of the most common congenital craniofacial malformations in the clinic, with an average prevalence of 2–7 per 10,000 newborns [1–3]. Auricles, as one of the main facial features, deformities or defects will seriously affect the physical and psychological health of children [4,5]. At present, the most commonly used treatment is auricular reconstruction based on autogenous costal cartilage carving scaffolds and artificial prostheses, in which the former will cause serious surgical trauma to the donor area and without precise auricular morphology, while the latter easily triggers foreign body reactions without biological function [6–8]. Therefore, the key bottleneck of auricular reconstruction is how to obtain ear reconstruction equivalents with accurate morphology and biological function.

The rapid development of tissue engineering and regenerative medicine has brought a new strategy for ear reconstruction [9–11], and

our group has realized the first international clinical breakthrough of tissue-engineered auricles based on polyglycolic acid/polylactic acid (PGA/PLA) and chondrocytes [12]. However, the patients showed varying degrees of inflammation and deformation after reconstructive surgery, which seriously hindered its clinical application. This may be due to the following reasons: (1) residual PGA/PLA polymer materials easily trigger aseptic inflammation, which astricts the formation of extracellular matrix (ECM) [13]; (2) conventional cell seeding techniques have difficulty achieving well distribution of chondrocytes, which affects the uniformity of ECM [14]; and (3) heterogeneous cartilage ECM aggravates insufficient mechanical stability and leads to deformation. Recently, natural hydrogels (such as gelatin, collagen, alginate, hyaluronic acid, etc.), which can effectively alleviate the aseptic inflammatory reaction problem, have become the research hotspot of tissue engineering scaffolds [15–17]. Three-dimensional (3D) bioprinting technology, which enables precisely defining the spatial distribution of cells and materials, has significant application advantages in the biomimetic construction of tissues and organs [18–22]. Therefore, the integration of hydrogels and bioprinting technology may be the key breakthrough to address the above problems. Nevertheless, the common hydrogels used to construct auricle equivalents have the following deficiencies: (1) the single components of conventional hydrogels have difficulty accurately mimicking the cartilage-specific microenvironment [23]; (2) the dense texture of the solidified hydrogels hinders the exchange of nutrients and affects the formation of internal cartilage tissue [24]; and (3) insufficient mechanical stability of hydrogels is not enough to maintain the fidelity of 3D morphology [25].

To overcome the above challenges, we present a novel strategy for the development of biological auricular equivalents with precise shapes and excellent mechanics using a bioactive bioink based on methacrylate-modified acellular cartilage matrix (ACMMA), with the assistance of gelatin methacrylate (GelMA), poly(ethylene oxide) (PEO), and polycaprolactone (PCL), by the integration of multi-nozzle 3D bioprinting technology. Photocrosslinkable ACMMA, prepared by enzymolysis and modification, is used to emulate the intricacy of the native microenvironment because of its similar component and composition to native tissues [26–28]. The auxiliary GelMA is used to balance the printability and stability of bioink, as well as to replenish some of the collagen components lost during decellularization [29,30]. PEO is introduced as a porogen and allows for the generation of micropores [31,32], which allow nutrient exchange and promote cell behavior. PCL with high strength and slow degradation is introduced as a grid frame to provide sufficient mechanical support for higher morphological fidelity [24,33]. 3D bioprinting technology enables precise control of the distribution of chondrocyte-laden bioink and PCL to fabricate auricular equivalents with precise shape and satisfactory mechanics [34]. Finally, the feasibility of auricular equivalents for regenerating auricular cartilage will be explored by evaluating its formation quality, tissue integration, biomechanical performance, and shape fidelity. It is anticipated that this innovative strategy of constructing biological auricular equivalents based on biomimetic microporous photocrosslinkable cartilage-derived ECM will provide new opportunities and reliable scientific evidence for the fabrication and regeneration of patient-specific cartilage such as the ear, nose, trachea, and meniscus.

## 2. Materials and methods

### 2.1. Materials and animals

All chemicals were reagent grade and supplied by Sigma–Aldrich (St. Louis, USA) unless otherwise stated. GelMA and lithium phenyl-2,4,6-trimethyl benzoyl phosphinate (LAP) were purchased from SunP Biotech (Beijing, China). Bama miniature pigs (female, 6 months old), Japanese white rabbits (female, 2 months old), and nude mice (male and female, 6 weeks old) were purchased from Beijing Vital River Laboratory Animal Technology Co., Ltd. (Beijing, China). Animal experiments were approved by the Animal Care and Experiment Committee of Plastic Surgery Hospital (Institute), Chinese Academy of Medical Sciences & Peking Union Medical College (Beijing, China).

### 2.2. Preparation of acellular cartilage matrix (ACM)

Auricular cartilage was isolated from Bama miniature pigs under aseptic conditions. After carefully removing the skin, the remaining ear cartilage tissues were cut into small pieces. The obtained cartilage pieces were rinsed using precooled aseptic deionized water and ground into powders using an automatic sample freeze-grinding machine (Shanghai Jingxin Co., Ltd, China). Cartilage powders were sequentially treated with 0.5% trypsin/phosphate-buffered saline (PBS), nuclease solution (containing 50 U/ml deoxyribonuclease and 1 U/ml ribonuclease A in 10 mM Tris-HCl, pH = 7.5), 10 mM Tris-HCl (including 10 U/ml aprotinin), and 1% Triton X-100/PBS solution for decellularization, as previously described [14,35]. Following the freeze-drying process, 10 mg/ml of the decellularized cartilage powder was enzymatically digested in 2 mg/ml collagenase solution at room temperature for 24 h with continuous stirring to form a flowable viscous solution. The viscous solution was terminated and dialyzed with a 3,500 D dialysis membrane in deionized water for 72 h. Finally, the prepared ACM was freeze-dried and stored at −20 °C until use.

### 2.3. Proteomic analysis of acellular cartilage matrix

To prepare the samples for proteomic analysis, both ACM and native cartilage powders were dissolved and cracked to extract protein. After leveling the protein level between samples, each protein sample was digested with trypsin and incubated at 37 °C. The resultant peptide samples were desalted by a Strata X C18 column and resuspended. After centrifugation, 10 μL of supernatant was subjected to a Q Exactive™ LC–MS/MS system (Thermo Fisher Scientific) as described previously [36,37]. The MS spectra were searched against the UniProt Sus scrofa (pig) reference proteome FASTA file using Protein Discover 2.2 software. A decoy database containing reverse sequences of the proteins was also used. The resultant peptides were assembled into protein groups, and only proteins with at least two distinct peptides were considered reliable. The ratio of the mean of the relative quantification values of all biological replicates for each protein in the comparative sample pair was taken as the fold change (FC). T-test was performed on the relative quantitative value of each protein in the two comparison samples, and the corresponding P value was calculated as a significance indicator. Protein difference analysis and hierarchical clustering analysis were performed to screen the high-retention proteins (FC > 2.0 and P value < 0.05) and low-retention proteins (FC < 0.50 and P value < 0.05). Gene symbols for identified proteins were uploaded to the web-based String tool to retrieve protein–protein interaction network data. Finally, a hypergeometric test was used to perform Gene Ontology (GO) analysis and Kyoto Encyclopedia of Genes and Genomes (KEGG) pathway analysis on the identified proteins to determine the biological functions of the differential proteins.

### 2.4. Methacrylation of acellular cartilage matrix

To prepare a photocrosslinkable hydrogel, ACM was modified by methacrylic anhydride (MA) as previously described [38,39]. Briefly, 0.5 g water-soluble ACM was dissolved in deionized water, and 0.5 mL MA was added at a rate of 0.5 mL/min in an ice bath. The pH was maintained between 8 and 10 by 5 M NaOH, and the reaction continued overnight under constant stirring. After the reaction, the solution was neutralized with 1 M HCl and dialyzed using a 3,500 D dialysis membrane in distilled water for one week, followed by freezing and lyophilizing.

## 2.5. Preparation of ACMMA-based hydrogels with microporous structures

The pre-gel solution was prepared 12 h prior to cell encapsulation. Briefly, both lyophilized ACMMA and GelMA were fully dissolved in culture medium to reach final ACMMA and GelMA concentrations of 5%, respectively. LAP powder, a photoinitiator, was fully dissolved in the solution to reach a final LAP concentration of 0.25%. PEO (average Mw = 300,000) powder, a pore-forming agent, was dissolved in the solution to reach a final PEO concentration of 1%. Based on the phase-separation void-formation strategy, an aqueous two-phase emulsion of two biocompatible solutions of ACMMA/GelMA and PEO polymers were adopted together to prepare microporous hydrogels upon subsequent photo-crosslinking and leaching procedures. All hydrogel formulations were fully mixed with continuous stirring, sterilized with syringe filters (0.45 μm pore size), and kept in an incubator to avoid light. Finally, photocrosslinkable hydrogel formulations were induced by exposure to blue light (wavelength: 405 nm; light source: LED (Uvata Precision Optoelectronics Co., Ltd.); intensity: 20 mW/cm$^2$; distance: 10 cm; exposure time: 60 s).

## 2.6. Characterization and rheology of microporous hydrogels

The structures of ACMMA, GelMA, hydrogel formulation precursors, and photocuring constructs were characterized and compared with $^1$H NMR experiments. $^1$HNMR spectra were recorded on a Bruker 400 MHz NMR spectrometer, and chemical shifts were reported in parts per million (ppm). To observe the microstructure of hydrogel formulations with or without micropores, hydrogels were conjugated with rhodamine B and observed under a confocal microscope (Leica TCS SP8 CARS). The surface morphology of the hydrogel constructs with or without microporous structure was observed using scanning electron microscopy (SEM, Philips XL-30, Amsterdam, Netherlands) at an accelerating voltage of 15 kV after being lyophilized and sputter-coated with gold. And the pore size and the porosity of the hydrogel constructs with or without microporous structure were analyzed by ImageJ software (n = 5 per group).

Rheological analysis was used to evaluate the photocuring performance of the gel precursor, and the viscosity and shear-thinning behavior were tested to evaluate its printability as the bioink [40]. Dynamic rheology experiments were performed on a HAAKE MARS III photorheometer equipped with a 20 mm diameter parallel plate geometry and OmniCure Series 2000. A time sweep oscillatory test was performed at a 10% strain (CD mode), 1 Hz frequency, and a 0.5 mm gap for 180 s. The gel point was determined as the time when the storage modulus (G′) surpassed the loss modulus (G″), and the shear modulus was determined as the G′ reaching complete gelation. Shear-thinning behavior was characterized in rotational tests at a gap of 500 μm, and the shear rate was increased logarithmically from 0.01 to 60 1/s. The gelation kinetics of the bioink were measured in the range of 1 °C–40 °C. All tests were performed at 25 °C except where otherwise stated, and each test was repeated five times with a new sample.

*In vitro* enzyme-mediated degradation of hydrogels was examined by a gravimetric method, as described in previous research [41]. Briefly, the above photocuring hydrogels (n = 5 per group) were weighed after lyophilization as the initial weight ($W_i$) and then placed in sterile PBS containing 20 U/mL hyaluronidases (hyaluronidase from bovine testes). Degradation was carried out at 37 °C, and samples were weighed after lyophilization as $W_t$ every other day until fully degraded. The degradation ratio was defined based on the percentage of mass loss according to the following equation:

$$Mass\ loss\ (\%) = \frac{W_i - W_t}{W_i} \times 100\%$$

## 2.7. Isolation and cultivation of auricular chondrocytes

Auricular cartilage was obtained from Japanese white rabbits and minced into 1 mm$^3$ piece under aseptic conditions. The cartilage pieces were washed with PBS and digested with 0.15% collagenase type II to isolate chondrocytes under gentle agitation at 37 °C, as previously established methods [42]. Then, the cells were harvested, cultured, and expanded in high glucose Dulbecco's modified Eagle medium (DMEM, Gibco, Grand Island, NY) containing 10% fetal bovine serum (FBS, Gibco, Grand Island, NY) and 1% penicillin–streptomycin-neomycin antibiotic (PSN, Gibco, Grand Island, NY) at 37 °C with 95% humidity and 5% CO$_2$. Chondrocytes in the second passage were harvested for further experiments.

## 2.8. Cell migration, viability, proliferation, and cell cycle analysis

To assess cell migration, nonporous and porous hydrogels embedded with chondrocytes ($1 \times 10^6$ cells/mL) were photocured on one side of confocal petri dishes, and the other side was coated with cell-free hydrogels [43]. After 7 days of culture, the living cells were stained with Calcein AM, and cell migration at the interface was observed under a confocal microscope.

Following 1, 7, and 14 days of culture, the viability of chondrocytes encapsulated in hydrogels with or without microporous structures was evaluated using the Live and Dead Cell Viability Assay (Invitrogen, USA) following the manufacturer's instructions and examined by confocal microscopy [14]. Three randomly selected visual fields were used to quantify cell viability with ImageJ software. In addition, DNA content was also used to further assess cell proliferation capacity using a total DNA quantification assay (PicoGreen dsDNA assay, Invitrogen, USA).

Cell cycle analysis was performed to further assess cell proliferation. After 7 days of culture, chondrocytes encapsulated in hydrogels with or without microporous structures were digested with 0.1% collagenase. Chondrocytes were collected, washed with precooled PBS, and treated with 70% ethyl alcohol at 4 °C for 24 h. Then, chondrocytes were stained with 50 μg/mL propidium iodide (PI) containing 10 μg/mL RNase at 37 °C for 30 min away from light. The cell cycle distribution was measured using a BD FACS Celesta Flow Cytometer (BD Biosciences, San Jose, California, USA), and the data were analyzed using Modfit LT 4.0 software [44].

## 2.9. Bioprinting of lattice-shaped cell-laden constructs and cartilage formation in vivo

Hydrogel formulation precursors with or without micropores were prepared as described above: (a) porous bioink: ACMMA/GelMA/PEO containing 5% ACMMA, 5% GelMA, 1% PEO, and 0.25% LAP; (b) nonporous bioink: ACMMA/GelMA containing 5% ACMMA, 5% GelMA, and 0.25% LAP. Auricular chondrocytes were collected and mixed with the above two kinds of bioink to reach a concentration of $20 \times 10^6$ cells/mL. The bioprinting process was completed using a 3D-Bioplotter (Envision TEC, Germany), and the printing parameters are shown in Table S1. During the bioprinting process, the photocrosslinkable bioink was solidified under constant irradiation from the blue light source. After bioprinting, two groups of cell-laden constructs were immersed in a culture medium for 24 h to dissolve PEO to form porous structures and then transplanted to both sides of the backs of nude mice to observe cartilage formation *in vivo*.

## 2.10. Bioprinting and regeneration of auricular cartilage

The 3D digital models of human auricula were prepared by 3D laser scanning and a computer-aided design system (CAD, 3DPRO Technology Co., Ltd, Shanghai, China), as previously described [45,46]. The bioprinting of the auricular digital models included two patterns: (a) 3D bioprinting of auricular constructs according to the parameters of

Printing Type 1 (cell-laden bioink); (b) 3D bioprinting of auricular constructs with PCL support by alternately printing between Printing Type 1 (cell-laden bioink) and Type 2 (PCL). Multi-nozzles and temperature control systems were used for bioprinting, and the printing parameters of the auricular digital models are shown in Table S2. On the printing platform at 20 °C, the low-temperature nozzle was used to extrude cell-laden bioink at 20 °C to form auricular constructs. For the auricular constructs with PCL support, the other high-temperature nozzle was used to fuse-deposit PCL at 65 °C for alternating printing on each layer. The 10 s interval between each layer was intended for blue light crosslinking of bioink while for cooling of PCL. After bioprinting and crosslinking, auricular constructs with or without PCL support were cultured in the medium for 24 h to remove PEO and then subcutaneously transplanted into nude mice to regenerate auricular cartilage tissues *in vivo*.

### 2.11. Three-dimensional reconstruction and morphological analysis of regenerated auricular cartilage

After 24 weeks of culture *in vivo*, regenerated auricular cartilage tissues with or without PCL support were collected and scanned by the Quantum GX Micro Computed Tomography (micro-CT) Imaging System (PerkinElmer, USA) to obtain DICOM files. The DICOM files were imported into Mimics Medical software (version 21.0, Materialise, Belgium) for 3D reconstruction to generate STL files. Both 3D reconstruction model files and initial digital model files were input into Geomagic Control software (version 2015). The initial digital model was set as a *reference,* while the 3D reconstruction model was set as a *test.* After fitting and alignment, the morphological similarity of the two models was analyzed by 3D deviation comparison and displayed in the form of a deviation chromatogram [47,48].

### 2.12. Histological, immunohistochemical, and immunofluorescence analyses

Specimens were collected and subjected to histological and immunohistochemical analyses as described previously [42]. Briefly, samples were fixed in 4% paraformaldehyde, embedded in paraffin, and sectioned. Then, sections were stained with H&E, safranine-O, and Alcian blue to evaluate the histological structure and cartilage-specific ECM deposition in the regenerated tissue. The expression of type II collagen was detected using a mouse monoclonal antibody against collagen II (MS-306-P1, 1:200, Invitrogen, USA), followed by a horseradish peroxidase-conjugated anti-mouse antibody (1:200, Dako, Denmark). Both antibodies were diluted in PBS and then colorized with diaminobenzidine tetrahydrochloride (DAB, Dako). For immunofluorescence analyses, sections were incubated with a mouse monoclonal antibody against Ki67 (ab245113, 1:200, Abcam, Cambridge, UK) and a rat monoclonal antibody against alpha-tubulin (ab6160, 1:200, Abcam, Cambridge, UK). Then, the sections were incubated with a goat polyclonal secondary antibody against mouse IgG-H&L (Alexa Fluor® 488) (ab150113, 1:500, Abcam, Cambridge, UK) and a goat polyclonal secondary antibody against rat IgG-H&L (Alexa Fluor® 594) (ab150160, 1:500, Abcam, Cambridge, UK). Finally, nuclei were counterstained with DAPI, and fluorescence images were recorded using a fluorescence microscope (Leica DM IRB).

### 2.13. Biochemical and biomechanical analysis

Specimens (n = 5) were collected and minced to conduct cartilage-related biochemical evaluations for DNA content, glycosaminoglycan (GAG) content, total collagen content, collagen II content, and elastin content using previously established protocols [41]. Briefly, DNA content was measured using the Quant-iT™ PicoGreen® dsDNA assay, GAG content was determined using the dimethylmethylene blue assay, and the total collagen content was detected using the hydroxyproline assay

kit (Nanjing Jiancheng Bioengineering, China). The proteins expression such as collagen II and elastin were determined using ELISA kits. The expression of cartilage-specific genes such as collagen type II alpha 1 (COL 2A1), aggrecan (ACAN), elastin (ELN), SRY-box transcription factor IX (SOX 9) was analyzed quantitatively with the SYBR Green using LightCycler® 96 Real-Time PCR system (Roche Ltd) according to a previously established method. Forward and reverse primer sequences were designed based on published gene sequences from NCBI and PubMed (Table S3). The relative expression levels for each gene were normalized with GAPDH and analyzed by the $2^{-\Delta\Delta CT}$ method. Young's modulus was analyzed using a biomechanical analyzer (Instron-5967, Canton, MA, USA) and all samples (n = 5) were processed to a cylindrical shape (8 mm in diameter and 2 mm in thickness) via refinement. A constant compressive strain rate of 0.5 mm/min was applied until 80% of the maximal deformation, and Young's modulus was calculated based on the slope of the stress–strain curve. For the compression relaxation test, the samples were compressed until the strain reached 10%, and the samples were allowed to relax for 10 min while maintaining the stress. And the stress relaxation slope was measured from the linear slope of the stress relaxation curve over the last 100 s. For the multi-cycle compression test, the samples were sequentially increased to 60% strain according to the 10% strain gradient, and the compression cycle was repeated 5 times at each gradient point. During all tests, a humidifier was used to maintain the humidity of the surrounding environment.

### 2.14. Statistical analysis

All quantitative data were collected from at least three repeated experiments and presented as the means ± standard deviation. Following confirmation of a normal distribution of the data, Student's t-test or one-way analysis of variance (ANOVA) was used to determine the statistical significance using GraphPad Prism 8.0 software, and a value of $P < 0.05$ was considered statistically significant.

## 3. Results and discussion

### 3.1. Characterization of photocrosslinkable acellular cartilage matrix hydrogels

ACM has been considered one of the most promising biomaterials to emulate intricacy in the native microenvironment because of its similar component and composition to native tissues [26,28]. The goals of decellularization are maximal clearance of cellular and genetic molecules and minimal loss of ECM components. In this study, porcine auricular cartilage was prepared into ACM by decellularization and enzymolysis procedures (Fig. 1A). DNA content was determined to validate the residual cellular components, and the cellular components in ACM (10.26 ± 2.03 ng/mg) were significantly decreased compared with native cartilage (209.80 ± 22.12 ng/mg, ***$p < 0.001$). To confirm ECM preservation, the contents of GAG and collagen in the ACM were quantified, and the retention rates were 56.86% and 49.34%, respectively (Fig. 1B). Additionally, to identify the ECM components retained after decellularization procedures, ACM and native cartilage were processed for proteomics analysis and revealed that 490 unique proteins were found solely in native cartilage, 27 unique proteins were found solely in ACM, and 587 proteins were found in both native and decellularized tissues (Fig. 1C), among which 54 proteins were significantly high-retention (FC > 2, P value < 0.05) and 81 proteins were significantly low-retention (FC < 0.5, P value < 0.05) by Volcano plot analysis (Fig. 1D). Hierarchical cluster analysis revealed clearly separate clustering of proteins found in ACM versus native cartilage, indicating that the proteome of acellular cartilage had substantial changes compared with that of native cartilage (Fig. 1E). The protein–protein interaction networks showed that some important cartilage-specific ECM, such as COL2, COL9, COMP, and ACAN had no difference between the ACM and native cartilage, while ELN and LOX, the important elastin fiber
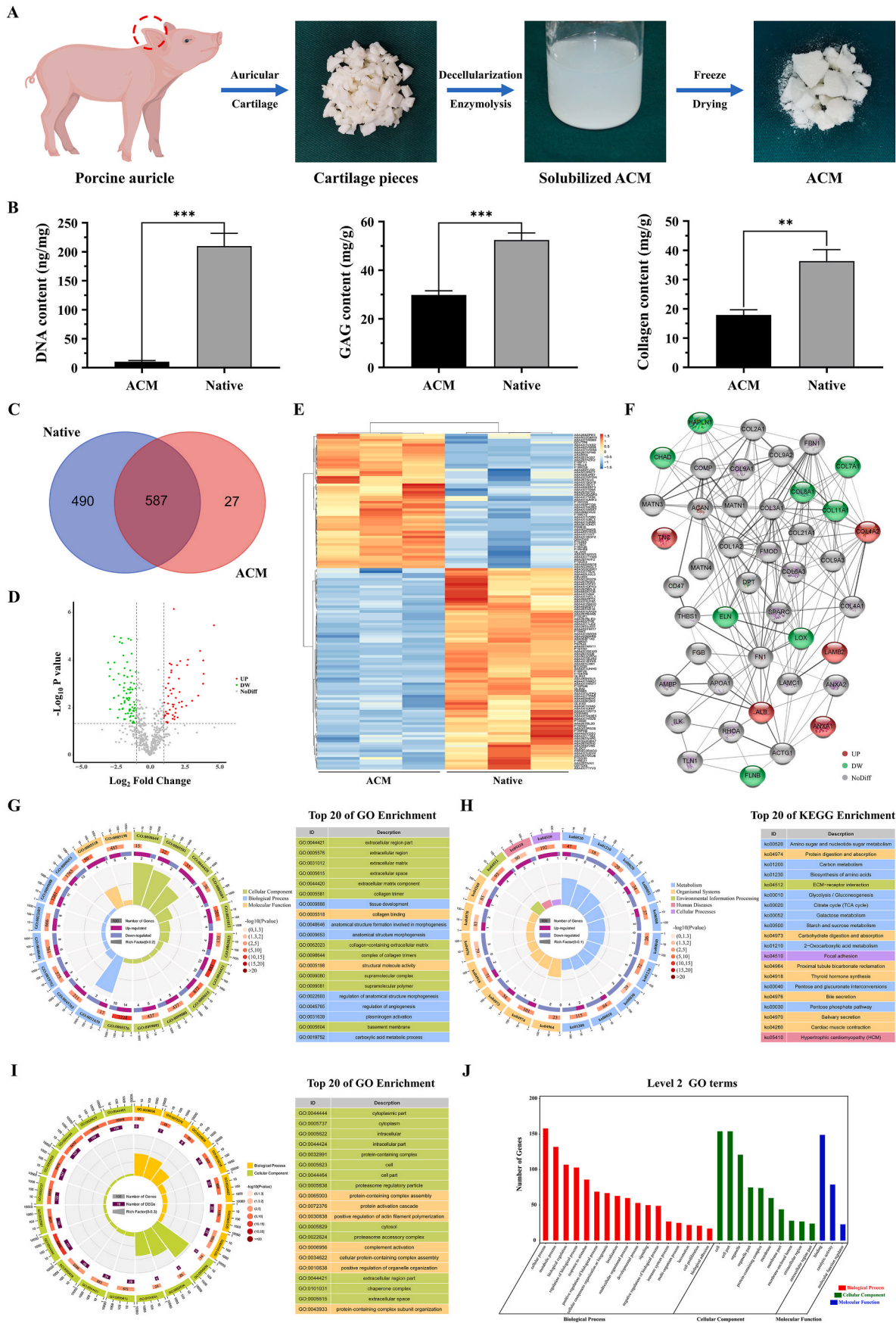
(caption on next page)

**Fig. 1.** Preparation and proteomic analysis of acellular cartilage matrix. A) Preparation of ACM by decellularization and enzymolysis procedures. B) Quantitative analysis of DNA content, GAG content, and collagen content. C) Venn diagram showing the number of proteins identified in native and ACM tissues. D) Volcano plot showing the significantly high-retention (red dots, FC > 2, P value < 0.05) and low-retention (green dots, FC < 0.5, P value < 0.05) proteins in ACM versus native cartilage. E) Heatmap and hierarchical cluster analysis using protein expression data from ACM and native tissues. Notice the biological variation in both ACM and native tissue samples (orange). F) Protein–protein interaction network of preserved proteins mainly associated with ECM in ACM (red represents high-retention proteins, green represents low-retention proteins). G) GO enrichment analysis and H) KEGG enrichment analysis of the differentially reserved proteins in the ACM and showing the top 20 enrichment terms. I) GO enrichment analysis of the lost proteins in ACM and showing the top 20 GO enrichment terms and J) top 30 of level 2 GO terms. **$p < 0.01$. ***$p < 0.001$. (For interpretation of the references to color in this figure legend, the reader is referred to the Web version of this article.)
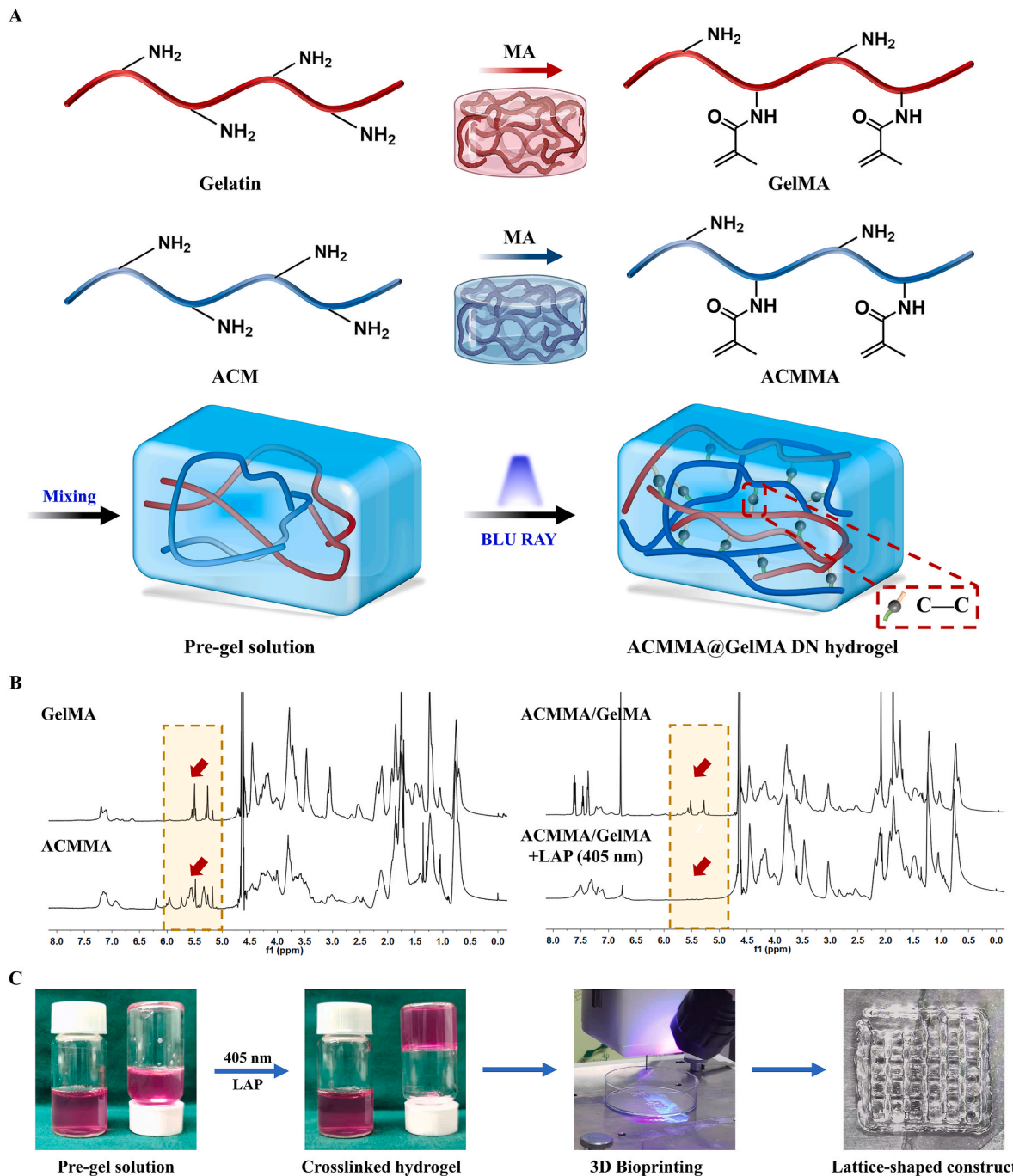


**Fig. 2.** The methacrylation mechanism and photocrosslinking process of methacrylated acellular cartilage matrix hydrogels. A) The methacrylation mechanism of GelMA and ACMMA, as well as the photocrosslinking mechanism from the flowable pre-gel solution to cured hydrogels under blue light irradiation (405 nm, 20 mW/cm²). B) ¹H NMR spectra of GelMA, ACMMA, and the photocrosslinking process of the ACMMA/GelMA gel precursor (the red arrows indicate the methacrylamide group signal peaks at 5.4 and 5.6 ppm). C) The photocrosslinking process and bioprinting process of lattice-shaped constructs based on ACMMA-based bioink. (For interpretation of the references to color in this figure legend, the reader is referred to the Web version of this article.)

assembling components decreased in ACM compared with native cartilage(Fig. 1F). Interestingly, there were 27 unique proteins found solely in ACM, and most of them were identified as uncharacterized proteins when searching the database. We speculated that this might be caused by the fact that the samples were digested into different peptide fragments during the digestion process and matched to different proteins.

Furthermore, GO enrichment analysis was conducted and the results showed that the reserved proteins in the ACM were mainly concentrated in *collagen trimers* and *extracellular matrix component* in cellular component, and related to *collagen binding* and *structural molecule activity* in molecular function (Fig. 1G). In addition, KEGG pathway results indicated that the upregulated proteins in ACM were mainly enriched in *focal adhesion* and *ECM-receptor interaction* pathways (Fig. 1H), which confirmed that the ACM reserved most ECM components and played important biological functions. Furthermore, to identify protein components that were lost during the decellularization process, GO enrichment analysis and level 2 GO terms showed that most of the lost components were related to cellular components, such as *cell, organelle, cytoplasm*, and *intracellular part*, which further verified the effectiveness of decellularization (Fig. 1I and J). In summary, the proteomics results verified that most ECM-related components were retained while cellular components were removed. Furthermore, the functional enrichment analysis on the differential proteins provided information for further compounding and modification to prepare more ideal biomimetic materials. It also provided strong evidence support for the application potential and advantages of biomimetic material of ACM in cartilage tissue engineering.

Despite such promising advances, the present ACM-based biomaterials have insufficient constructability and mechanical stability, which risks hampering practical applications for fabricating the desired 3D constructs [25,49]. To address this problem, ACM was modified with MA to prepare a methacrylate-modified ACM with rapid photocrosslinking properties. Fig. 2A illustrates the structure of the methacrylated ACM and the photocrosslinking mechanism from the flowable pre-gel solution of ACMMA to cured hydrogels under blue light irradiation (405 nm, 20 mW/cm$^2$). $^1$H NMR spectra were further performed to evaluate the methacrylated modification of photosensitive polymers and the photocrosslinking mechanism. After grafting MA into ACM, the methacrylamide group signal peaks increased at 5.4 and 5.6 ppm, indicating the successful modification of ACMMA (Fig. 2B). The substitution degree of ACMMA, determined by the integral ratio of the proton peaks at 5.2–6.2 ppm to the peak at 2.9 (amino groups of ACM) and 1.3 ppm (hydroxyl groups of ACM), indicated 83% of methacrylate-modified ACM. And the substitution degree of GelMA was determined by the integral ratio of the proton peaks at 5.2–6.2 ppm to the peak at 2.9 (amino groups of gelatin), indicted 94% of methacrylate-modified gelatin. However, ACMMA hydrogels have poor printability and physical properties, resulting in limited structural stability and shape fidelity. To address this issue, GelMA was added as an auxiliary to balance the printability and stability of bioink, as well as to replenish some of the collagen components lost during decellularization. Similarly, the $^1$H NMR trace of the photocrosslinking process of the ACMMA/GelMA hydrogel precursor showed that the signals of the gel precursor distinctly decreased at 5.4–7.8 ppm under blue light irradiation, indicating the successful photopolymerization mechanism of the GelMA/ACMMA hydrogel. Therefore, the ACMMA/GelMA hydrogels had suitable printability and could be printed into a lattice-shaped construct (Fig. 2C), which indicated that ACMMA/GelMA hydrogels could meet the requirements of printing fine structures and maintaining construct integrity. In addition, the cytotoxicity tests (CCK-8) of ACMMA/GelMA also showed satisfactory cell viability ($p > 0.05$), which proved that the MA-grafted hydrogels had no obvious toxicity to cell growth and survival (Fig. S1).
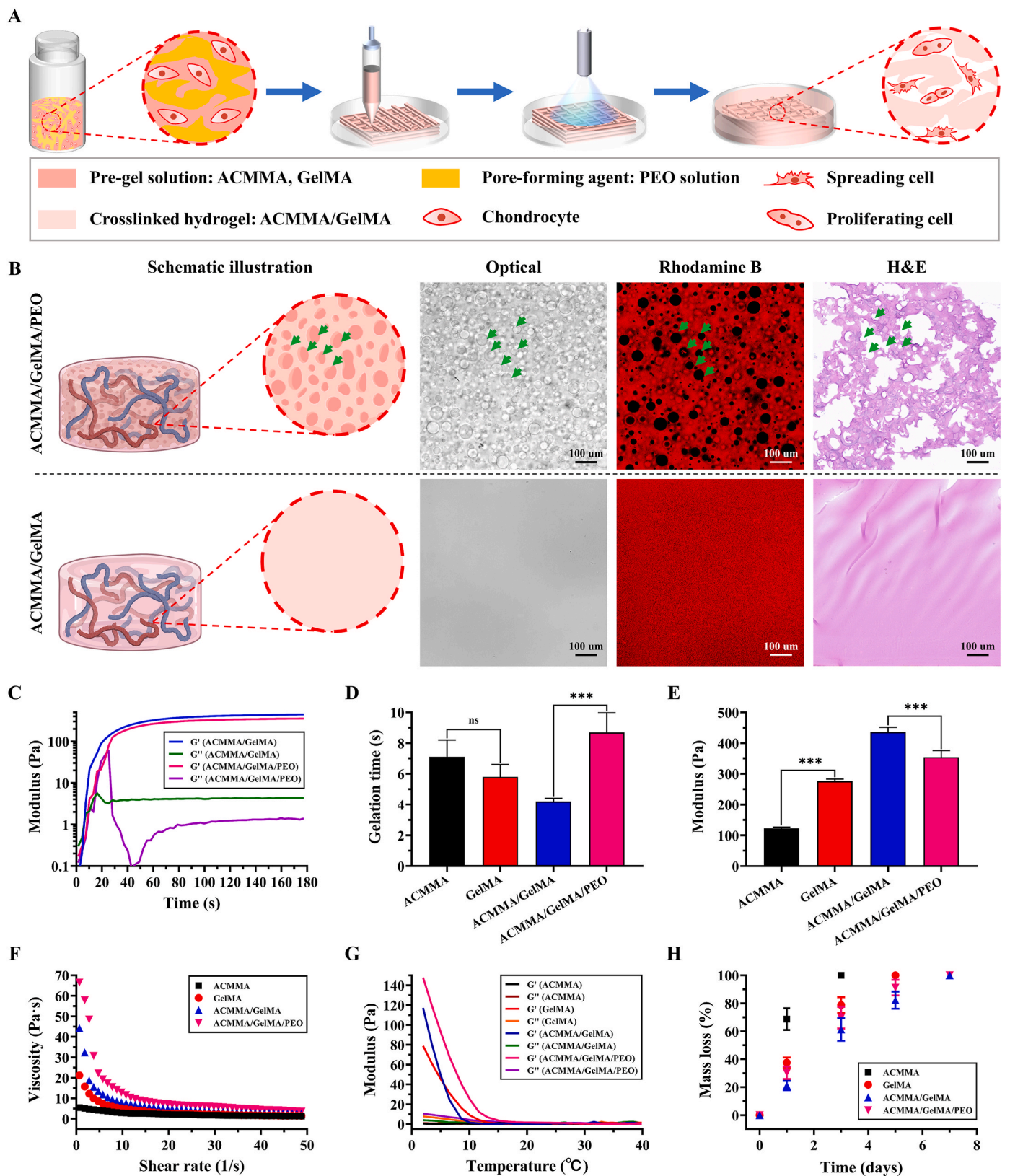
## 3.2. Physicochemical properties of microporous hydrogels

The dense texture of the crosslinked hydrogel will hinder the exchange of nutrients and metabolic waste, which in turn will affect the formation of internal cartilage tissue [50]. To solve this dilemma, PEO, a nontoxic and water-soluble bioinert polymer [31,32], was introduced as a porogen that allows for the generation of micropores in bioink. As shown in Fig. 3A, PEO was added into ACMMA/GelMA solution resulting in phase separation of ACMMA/GelMA and PEO aqueous solutions and thus creating voids in crosslinked ACMMA/GelMA hydrogel after removing uncrosslinked PEO droplets. To evaluate the pore-forming effect of PEO, the microporous structure of the hydrogel was analyzed after normal culture. Optical images, rhodamine B staining (the hydrogel networks conjugated with rhodamine B emitted red fluorescence, while dark areas indicated the micropores), and H&E staining all showed many micropores generated in the ACMMA/GelMA/PEO hydrogel (Fig. 3B). SEM examination further revealed the ultrastructure of the hydrogel, and the micropores structure formed by the PEO on the hydrogel could be clearly observed as indicated by the green arrows in Fig. S2 (the blue arrows indicated the micropores formed during the lyophilization of the hydrogel). Meanwhile, the pore size and the porosity of the porous hydrogel were also significantly higher than that of the non-porous hydrogel (***$p < 0.001$), and the pore size formed by freeze-drying was too small to be suitable for the proliferation and migration of chondrocytes, which further confirmed the pore-forming effect of PEO addition.

Rheological properties describe the deformation and flow of hydrogels under the influence of external forces, which are the physicochemical parameters influencing hydrogel printability [51]. In this study, the photocrosslinking process under blue light irradiation was investigated by dynamic rheological testing. As shown in Fig. 3C, the rheological tests demonstrated that G' exceeded G'' at the gel point within 10 s, indicating the excellent photocrosslinking performance of gel precursors. The complete crosslinking basically reached equilibrium at 60 s and the finial modulus was obtained according to the time-dependent sweep rheological experiments. There was no significant difference in gelling time between ACMMA and GelMA ($p > 0.05$), but the modulus of ACMMA was significantly lower than that of GelMA (***$p < 0.001$), which confirmed that ACMMA was not enough to maintain the structural integrity for a long time. For ACMMA/GelMA formulations, the formation of microporous structures led to the prolongation of gel time (***$p < 0.001$) and the decrease of modulus (***$p < 0.001$) (Fig. 3D and E), which is mainly affected by the microporous structure in hydrogels. Viscosity has a great influence on printing fidelity and cell viability. Generally, a higher viscosity leads to higher printing fidelity, but an increase in shear stress will affect the viability of cells in bioink. Therefore, the balance between viscosity and cell viability is very important for structural integrity and functionality [52]. As shown in Fig. 3F, the viscosity of ACMMA/GelMA gel precursors was controllable and decreased as the shear rate increased. This property of shear-thinning is suitable for printing cell-laden bioink without seriously affecting the survival of cells. Meanwhile, hydrogels showed high sensitivity to temperature, and the modulus increased rapidly when the temperature reached the gelation temperature (Fig. 3G), which indicated that they have good printing performance by adjusting the extrusive pressure, rate, and temperature. In addition, the results of the compression experiments showed that the addition of PEO had no significant effect on the compressive modulus and compressive relaxation ($p > 0.05$), but interestingly, it significantly reduced the multi-cyclic compressive strain loss (***$p < 0.001$), which might be attributed to the porous structure (Fig. S3).

Biodegradation is an essential property for hydrogel-based cartilage tissue engineering. As shown in Fig. 3H, all hydrogels were completely degraded within 7 days, indicating that hydrogels could be degraded by standard enzymatic mechanisms. Meanwhile, ACMMA/GelMA formulations exhibited a moderate degradation rate, which was more

**Fig. 3.** Physicochemical properties of microporous hydrogels. A) Schematics illustrating 3D bioprinted microporous hydrogels by dissolving PEO are beneficial to cellular behavior. B) The schematic illustration, as well as optical images, rhodamine B (the hydrogel networks conjugated with rhodamine B emitting red fluorescence, while dark areas indicate the micropores), and H&E showing the microporous structures compared with nonporous hydrogel. Rheological characteristics of bioink: C) Storage modulus (G') and loss modulus (G''), D) Gelation time, E) Shear modulus, F) Viscosity performance, and G) Temperature-sensitive properties. H) Enzyme-mediated degradation of bioink. ns: $p > 0.05$. ***$p < 0.001$. (For interpretation of the references to color in this figure legend, the reader is referred to the Web version of this article.)

conducive to maintaining the structural integrity of cell-laden constructs. On account of the above excellent rheological characteristics, proper mechanical strength, and moderate degradation rate, ACMMA/GelMA formulation precursors enable smooth extrusion and rapid photocrosslinking during 3D bioprinting, which further ensures the maintenance of precise shapes and integrity structures for cartilage regeneration.

### 3.3. Cell viability, migration, proliferation, and cell cycle evaluation

Balancing printability and cellular behavior have always been challenging, as important cellular processes, such as viability, migration, proliferation, and ECM deposition can be impeded when cells are embedded in dense polymer networks, while dense networks often support the best shape fidelity and long-term stability [53,54]. The performance of chondrocytes embedded in hydrogels was evaluated by cell viability, migration, proliferation, and cell cycle analysis. After 7 days of culture, cell migration testing showed that a large number of chondrocytes migrated to the side of cell-free hydrogels in the microporous hydrogels group (as shown by the green arrows in Fig. 4A), while no obvious cells were observed on the side of cell-free hydrogels in the nonporous hydrogels group, indicating that the microporous structure in hydrogel provides spatial space for cell migration. As shown in Fig. 4B, cellular viability assays showed that chondrocytes grew well (green fluorescence) in both porous and nonporous hydrogels with a significant increase in numbers over time, and only a small number of dead cells (red fluorescence) were observed at all observation times. Notably, the number of living cells in the ACMMA/GelMA/PEO group was significantly higher than that in ACMMA/GelMA group after culturing for 7d and 14d *in vitro* (Fig. 4C), suggesting that the microporous structures may be conducive to the diffusion and exchange of nutrients and metabolic wastes and in turn promote cell activity and proliferation.

Cell proliferation was further confirmed by Ki67 staining and cell cycle analysis. As shown in Fig. 4D, the number of Ki67-positive cells (green fluorescence) in porous hydrogels was higher than that in nonporous hydrogels. Meanwhile, the number of cells that were undergoing division (as indicated by the yellow arrows) in porous hydrogels was also higher than that in nonporous hydrogels. Furthermore, the cell cycle results in Fig. 4E showed that the proportion of cells occupying the S phase ($25.08 \pm 6.28\%$) and G2/M phase ($10.63 \pm 1.54\%$) in porous hydrogels was significantly higher than that in nonporous hydrogels (S phase: $2.59 \pm 0.87\%$, G2/M phase: $3.78 \pm 1.27\%$, $***p < 0.001$), which further confirmed the promoting effect of microporous structures on cell proliferation. Collectively, the above results confirmed that the microporous hydrogels were more favorable for cell migration and proliferation, indicating that the microporous ECM-based hydrogel provides a suitable 3D microenvironment for cell bioactivity.

### 3.4. In vivo cartilage regeneration with bioprinting lattice-shaped cell-laden constructs

The most important criterion for testing whether a biomaterial is suitable for tissue engineering is to evaluate tissue regeneration *in vivo*. The feasibility of cartilage regeneration with ACMMA/GelMA bioink-encapsulated chondrocytes was explored in nude mice. As shown in Fig. 5A, the cell-laden constructs in ACMMA/GelMA/PEO group formed preliminary cartilage-like tissue at 4 weeks *in vivo*, and histological staining showed more cells formed chondrocyte population with obvious cartilage-specific ECM deposition, while the constructs in ACMMA/GelMA group showed that isolated chondrocytes were scattered in hydrogels with a few pericellular matrix positive staining. After 8 weeks of culture, this phenomenon was more obvious. The cartilage-like tissues constructed by microporous hydrogel (ACMMA/GelMA/PEO group) showed cell population forming cartilage islands with increased deposition of ECM, while the tissues constructed with nonporous bioink (ACMMA/GelMA group) still showed isolated cells

and pericellular matrix (Fig. 5B). By 12 weeks, the tissues formed by porous hydrogels showed a milky-white cartilage appearance, and histology displayed a large amount of cartilage-specific ECM deposition and typical lacunae structure formation. In contrast, the cartilage-like tissues formed by nonporous hydrogels only exhibited pericellular matrix scattered in the hydrogel (Fig. 5C).

Consistent with gross appearance and histological examination, the quantitative analyses of biochemical revealed that GAG content, collagen content, and DNA content in engineered cartilage-like tissues gradually increased with increasing culture time (Fig. 5D), indicating that cartilage regeneration experienced a gradual maturation process *in vivo*. In addition, the content of the above components in regenerated cartilage from porous constructs was significantly higher than that in nonporous constructs in the same period ($*p < 0.05$). Notably, after the content of GAG and collagen normalized by DNA content (GAG/DNA, collagen/DNA), no statistically significant differences were observed in regenerated cartilage between porous and nonporous constructs at 4 and 8 weeks ($p > 0.05$), while a significant difference was evident at week 12 ($*p < 0.05$). These results revealed that the enrichment of GAG and collagen content in the early stage was mainly attributed to cell proliferation. In addition, the expression of cartilage-related proteins such as collagen II and elastin, as well as the cartilage-specific genes such as SOX 9, COL 2A1, ELN, and ACAN also showed the same trend, that is, the expression levels gradually increased with the prolongation of culture time, and the porous group was significantly higher than the non-porous group (Fig. S4). The biomechanical performance also showed the same trend as the biochemical performance. Young's modulus increased gradually with time, and the modulus of porous constructs was significantly higher than that of nonporous constructs. This might be explained by the fact that the porous structure was conducive to the proliferation of cells and the secretion of ECM, which in turn promoted the enhancement of biomechanical performance. All these results indicated that microporous hydrogels might not only be conducive to the exchange of nutrients and metabolic waste to maintain higher cell viability and proliferation but also provide a suitable 3D microenvironment for cell activity and function, which is more beneficial to the secretion of ECM and more conducive to the regeneration of mature cartilage tissue.

### 3.5. Bioprinting and regeneration of auricular cartilage using ACMMA-based microporous bioink

3D morphological cartilage formation is an important criterion to evaluate whether a scaffold can be used for cartilage tissue engineering. The prospect of 3D bioprinting techniques has reinvigorated strategies for tissue engineering, which can not only achieve the precise distribution of materials and cells but also complete the personalized customization of precise shapes [47,55]. The 3D digital model of the human auricle ($15.17 \times 26.01 \times 7.75$ mm), prepared by 3D laser scanning and CAD technologies, was successfully fabricated into cell-laden auricular constructs by a 3D bioprinting technique (Fig. 6A, Movie S1). After 7 days of culture *in vitro*, the Live/Dead staining showed that the chondrocytes encapsulated in microporous hydrogels had good viability (Fig. 6B).

Supplementary data related to this article can be found at https://doi.org/10.1016/j.bioactmat.2022.02.032.

After ensuring biocompatibility, the regeneration of auricular cartilage will become the focus of attention. The nude mouse model is the preferred method to examine whether mature auricular cartilage with satisfactory shape and excellent elasticity can be successfully regenerated *in vivo*. Then, auricular constructs were subcutaneously transplanted into nude mice, and after 12 weeks *in vivo*, the constructs largely maintained their original auricular shape (Fig. 6C). By 24 weeks, the cartilage-like tissue in the shape of a human auricle was successfully regenerated, which basically maintained its original shape. Importantly, the regenerated auricular cartilage could rapidly return to its original state without destruction when the external force was removed,
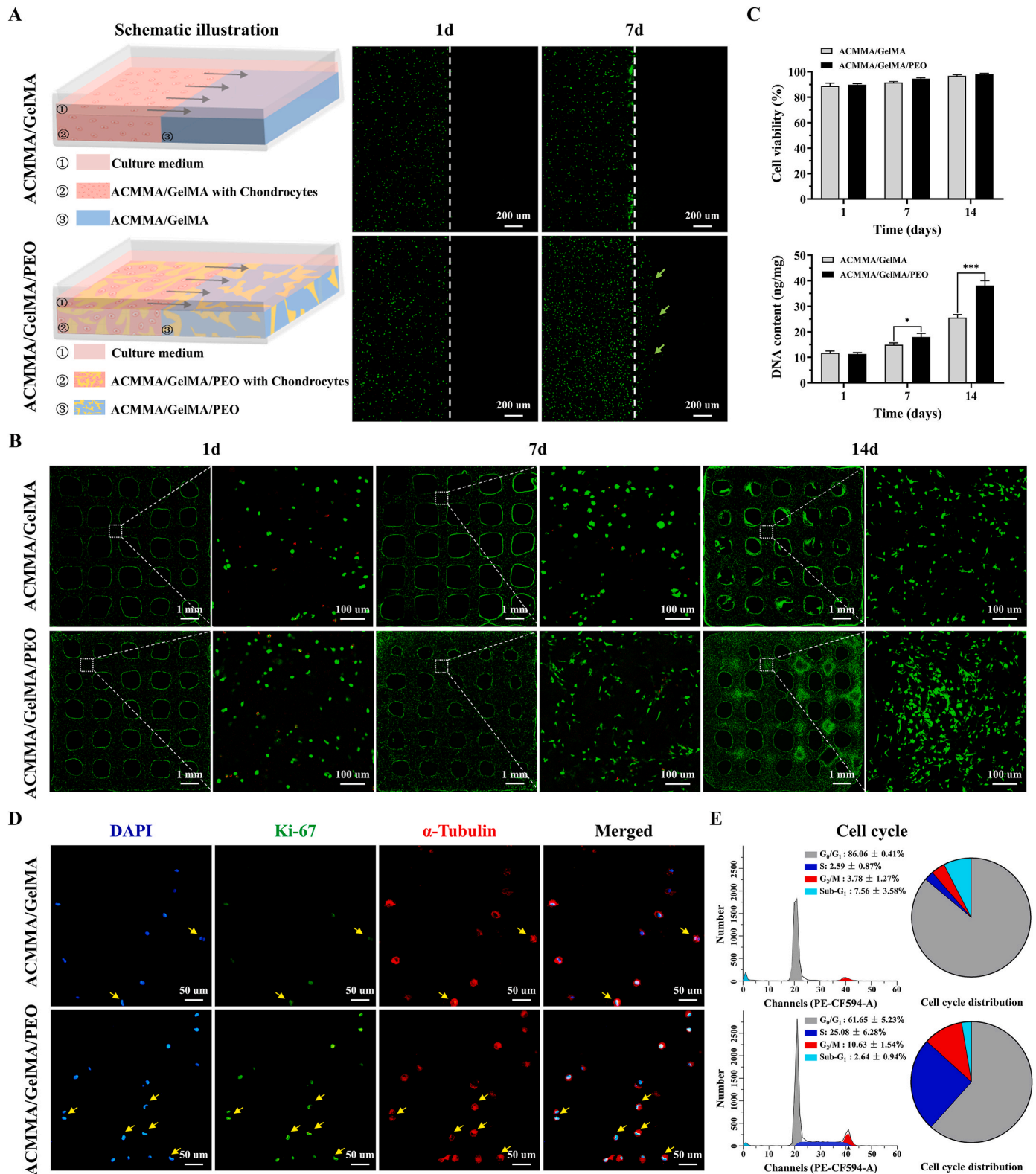
**Fig. 4.** Biocompatibility analysis of microporous bioink. A) Schematic illustration of cell migration tested by the Calcein-AM staining (the green arrows indicate cell migration). B) Live and Dead staining (green fluorescence and red fluorescence representing live cells and dead cells, respectively) and C) quantification of cell viability and DNA content of chondrocytes in cell-laden constructs. D) Immunofluorescence of Ki67 (green fluorescence representing proliferating cells and yellow arrows indicating cells undergoing division) and E) cell cycle analysis to evaluate cell proliferation. *$p < 0.05$. ***$p < 0.001$. (For interpretation of the references to color in this figure legend, the reader is referred to the Web version of this article.)
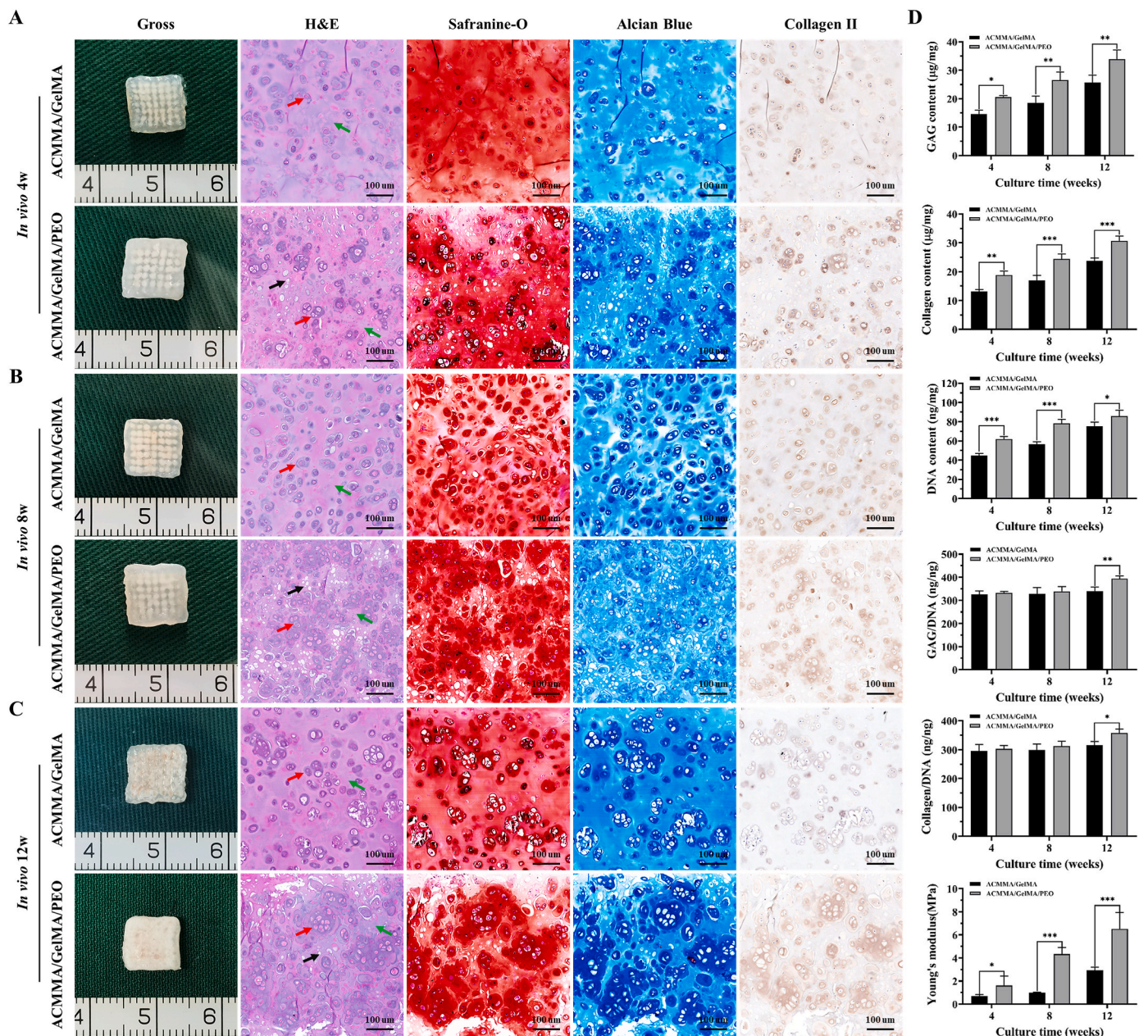
**Fig. 5.** *In vivo* cartilage regeneration with bioprinting lattice-shaped cell-laden constructs. Gross view and histological staining of H&E, Safranin-O, Alcian blue, and Collagen II staining of engineered cartilage-like tissues after A) 4 weeks, B) 8 weeks, and C) 12 weeks of culture *in vivo*. D) Biochemical and biomechanical quantitative evaluation of GAG content, collagen content, DNA content, GAG/DNA, collagen/DNA, and Young's modulus of regenerated cartilage-like tissues after 4 weeks, 8 weeks, and 12 weeks of culture *in vivo* (n = 5). Red arrows: cells or secreted ECM. Green arrows: residual hydrogel material. Black arrows: microporous structures. *$p < 0.05$. **$p < 0.01$. ***$p < 0.001$. (For interpretation of the references to color in this figure legend, the reader is referred to the Web version of this article.)

indicating that it had good elastic properties (Movie S2).

Supplementary data related to this article can be found at https://doi.org/10.1016/j.bioactmat.2022.02.032.

How to maintain the high shape fidelity of auricular constructs in long-term culture is an urgent issue to be solved in auricular tissue engineering. Ideally, the engineered construct should be matched in size and shape to the original digital model, which is prepared according to the requirements of the patients [47,48]. To quantify the maintenance of auricular morphology, the regenerated auricular cartilage was reconstructed by micro-CT (Movie S3) and analyzed by 3D deviation comparison. Morphological similarity was displayed in the form of a deviation chromatogram, and the deviation within ±1 mm and ±2 mm reached 86.69 ± 3.24% and 98.09 ± 0.76%, respectively (Fig. 6D),

indicating that auricular morphology was largely maintained during 24 weeks of culture. In addition, histological analysis of the cross-section further revealed that the auricular constructs formed mature cartilage-like tissue with abundant lacunae structure as well as strong positive staining of GAG and type II collagen (Fig. 6E).

Supplementary data related to this article can be found at https://doi.org/10.1016/j.bioactmat.2022.02.032.

*3.6. Bioprinting and regeneration of auricular cartilage using ACMMA-based microporous bioink with PCL support*

To further enhance the mechanical strength of the constructs to achieve better maintenance of 3D morphology, PCL with high strength
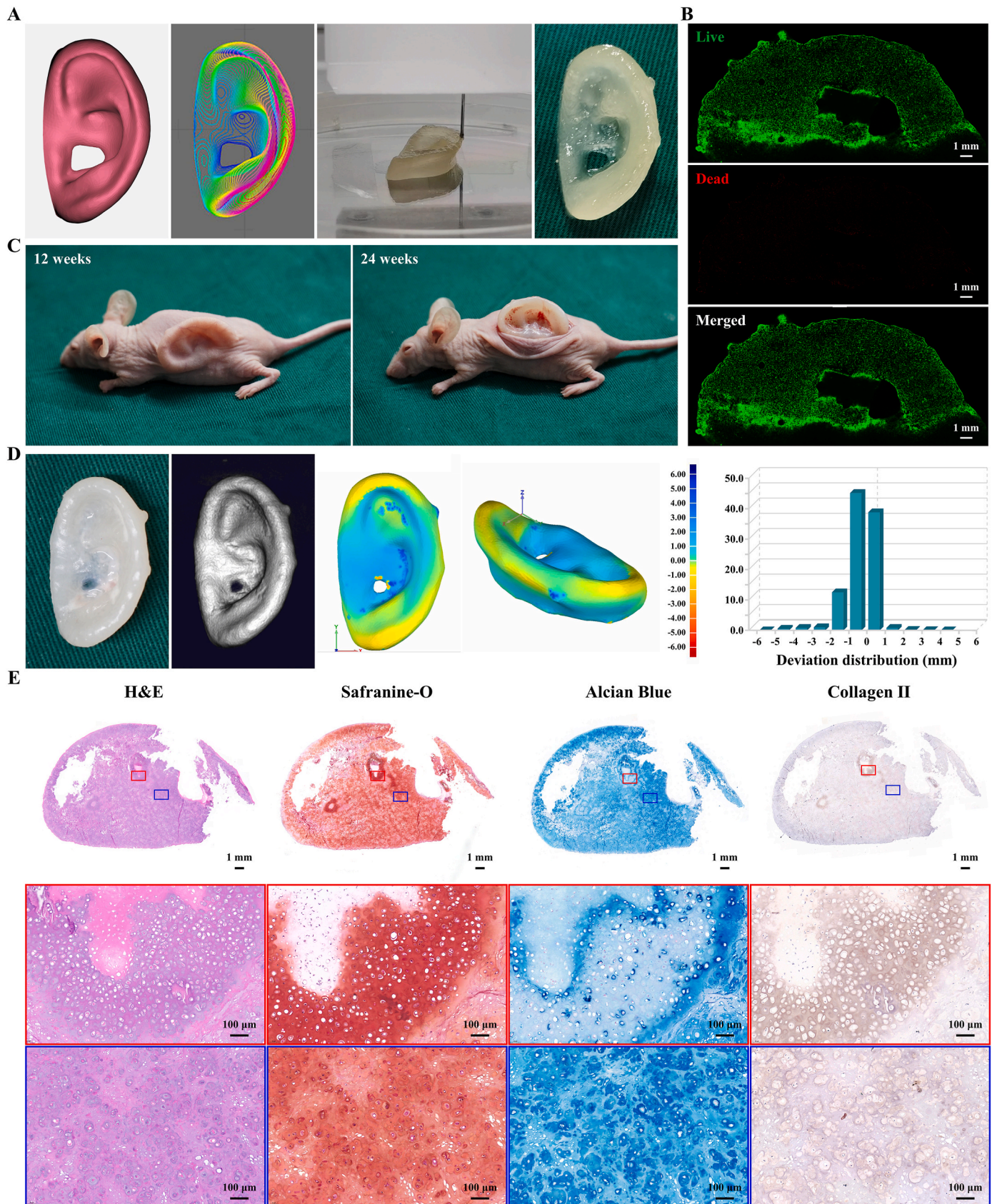
**Fig. 6.** Bioprinting and regeneration of auricular cartilage using ACMMA-based microporous bioink. A) The 3D digital model of human auricle and bioprinting auricular construct based on ACMMA-based microporous bioink. B) Live/Dead staining of bioprinted auricular constructs. C) Regenerating auricular cartilage after 12 and 24 weeks of culture in nude mice. D) 3D reconstruction and 3D deviation comparison of regenerated auricular cartilage. E) H&E, Safranin-O, Alcian blue, and Collagen II staining of regenerated auricular cartilage after 24 weeks of culture *in vivo*. (For interpretation of the references to color in this figure legend, the reader is referred to the Web version of this article.)

and slow degradation, which was approved by the Food and Drug Administration (FDA) for clinical application [24,33,56], was introduced as a grid frame to provide sufficient mechanical support. It has been reported that PCL has significant advantages in improving the mechanical strength and maintaining the 3D shape of engineered cartilage, which may be since PCL is considered a biosafety material in the clinic because of its slow degradation and rarely triggers immune or inflammatory reactions [57,58]. How to effectively integrate it with bioink and realize the directional distribution of materials and cells is a great challenge, which is extremely important for manufacturing homogeneous and refined auricular constructs.

The orderly coordination of different nozzles and materials must be coordinated at the same time to ensure the stability of the overall structure on the premise of ensuring high cell viability. To address this issue, the 3D digital model of the human auricle ($15.24 \times 24.03 \times 6.23$ mm) was designed as a hybrid structure with an alternating arrangement of bioink and PCL, which ensures that both sides of each PCL strand are wrapped with bioink to avoid direct contact with the body (Fig. 7A, Movie S4). In the process of layer-by-layer printing, each layer of PCL is deposited and hovered for 10 s to cool it and then deposit bioink to reduce the cell damage caused by the high temperature of PCL. In addition, the stability of the overall structure mainly depends on the bonding of intersecting PCL strands. Because of the hydrophobicity of PCL, the hydrogel not only cannot firmly combine with PCL but also affects the bonding between PCL strands. Therefore, each PCL strand in the printing model is modified to be reprinted twice to ensure that the height of the PCL strands exceeds the hydrogel in each layer to guarantee the solid bonding of the PCL between layers. After a series of parameter optimizations, auricular equivalents based on ACMMA-based microporous bioink and PCL were successfully fabricated by multinozzle bioprinting technology.

Supplementary data related to this article can be found at https://doi.org/10.1016/j.bioactmat.2022.02.032.

After 7 days of culture *in vitro*, the biocompatibility of auricular equivalent was evaluated by Live/Dead staining, and the results showed that chondrocytes grew well in hydrogels, indicating that the addition of PCL did not damage the viability of chondrocytes in bioink (Fig. 7B). After transplantation in nude mice for 12 weeks, the fine structure of the auricular construct was mostly maintained, indicating that the auricular construct with PCL support had enough mechanical properties to resist skin tension (Fig. 7C). By 24 weeks, the auricular cartilage-like tissue with an ivory-white cartilage appearance was successfully regenerated. Noticeably, the regenerated auricular cartilage with PCL support exhibited enough strength and stiffness that it was difficult to be deformed by an external force, indicating that the PCL played a great supporting role in resisting deformation (Movie S5). After 3D reconstruction (Movie S6), the morphology of the regenerated auricular cartilage was analyzed and displayed in the form of a deviation chromatogram. Compared with the original digital model, the deviation within $\pm 1$ mm and $\pm 2$ mm reached $94.14 \pm 1.34\%$ and $98.58 \pm 0.12\%$, respectively (Fig. 7D), which was significantly superior to that without PCL support. Meanwhile, histology showed that auricular constructs with PCL support formed mature cartilage-like tissue with typical lacunae structure and strong positive staining of cartilage-specific ECM (Fig. 7E).

Supplementary data related to this article can be found at https://doi.org/10.1016/j.bioactmat.2022.02.032.

The introduction of PCL significantly improved the shape fidelity of auricular equivalents (Fig. 8A and B), but the only deficiency was that the space occupation of slowly degraded PCL affected the formation and integration of engineered cartilage (Fig. 8C). Consistent with the histological results, the quantitative analysis (Fig. 8D–F) revealed that collagen content of regenerated auricular cartilage with or without PCL support reached over 85% of the native cartilage (*$p < 0.05$), while both GAG content and DNA content almost reached the level of native cartilage with no statistically significant difference ($p > 0.05$).

Meanwhile, the biomechanical performance showed that the modulus of regenerated auricular cartilage without PCL support reached over 65% of the native cartilage, while that of regenerated auricular cartilage with PCL support reached levels approximately 2.6-fold greater than native cartilage (*$p < 0.05$) (Fig. 8G and H). These results demonstrated that although the existence of the PCL had the problem of space occupation, it did not affect the formation of mature cartilage tissue in the bioink area while providing sufficient strength and stiffness support.

This work showed that auricular equivalents based on ACMMA-based microporous bioink with or without the PCL framework successfully formed mature auricular cartilage with high morphological fidelity, abundant cartilage lacunae, and cartilage-specific ECM deposition. The regenerated auricular cartilage without PCL support shows satisfactory elasticity; that is, it can rapidly return to the initial state when the external force is removed. The auricular cartilage with PCL support further improves the overall stiffness to avoid more deformation. This may be attributed to the significant increase in compressive modulus with the addition of PCL, but also loses some elastic properties due to increased multi-cyclic strain compressive loss (Fig. S3). It is noted that because of the spatial occupation of PCL, its distribution and parameters need to be further optimized, that is, to reduce the amount of PCL as much as possible while ensuring high morphological fidelity and excellent biomechanical performance. Additionally, due to the partial deficiency of the immune system, weakness skin tension, and different microenvironments in nude mice, this needs to be verified in large animal models in future research to explore its feasibility for preclinical application. Although these problems need to be optimized by further experiments, the current research has provided detailed supporting techniques and reference strategies for the construction of specially shaped cartilage, such as the ear, nose, trachea, and meniscus. Furthermore, it also provides reliable scientific evidence for the preclinical application of tissue-engineered cartilage in the future.

## 4. Conclusion

In summary, the current study prepared a microporous photocrosslinkable bioactive bioink based on cartilage-derived ECM with the assistance of GelMA and PEO. In addition, by integrating multi-nozzle 3D bioprinting technology to precisely control the distribution of chondrocyte-laden bioink and PCL, microporous auricular equivalents with precise shapes and satisfactory mechanical strength were successfully fabricated. Most importantly, mature auricular cartilage tissue with high morphological fidelity, excellent elasticity, abundant cartilage lacunae, and cartilage-specific ECM deposition was successfully regenerated in nude mice. Although the preparation parameters of auricular constructs and the feasibility of large animal models need to be optimized and verified by further experiments, the current research has provided detailed techniques and optimized strategies for the construction of patient-specific cartilage, as well as reliable scientific evidence for the preclinical application of tissue-engineered cartilage in the future.

## CRediT authorship contribution statement

**Litao Jia:** Conceptualization, Methodology, Data curation, Visualization, Software, Investigation, Writing – original draft. **Yujie Hua:** Conceptualization, Methodology, Data curation, Software, Investigation. **Jinshi Zeng:** Methodology, Data curation. **Wenshuai Liu:** Methodology, Visualization. **Di Wang:** Visualization. **Guangdong Zhou:** Conceptualization, Methodology, Funding acquisition, Supervision, Writing – review & editing. **Xia Liu:** Conceptualization, Methodology, Funding acquisition, Investigation, Supervision, Writing – review & editing. **Haiyue Jiang:** Conceptualization, Funding acquisition, Investigation, Supervision, Writing – review & editing.
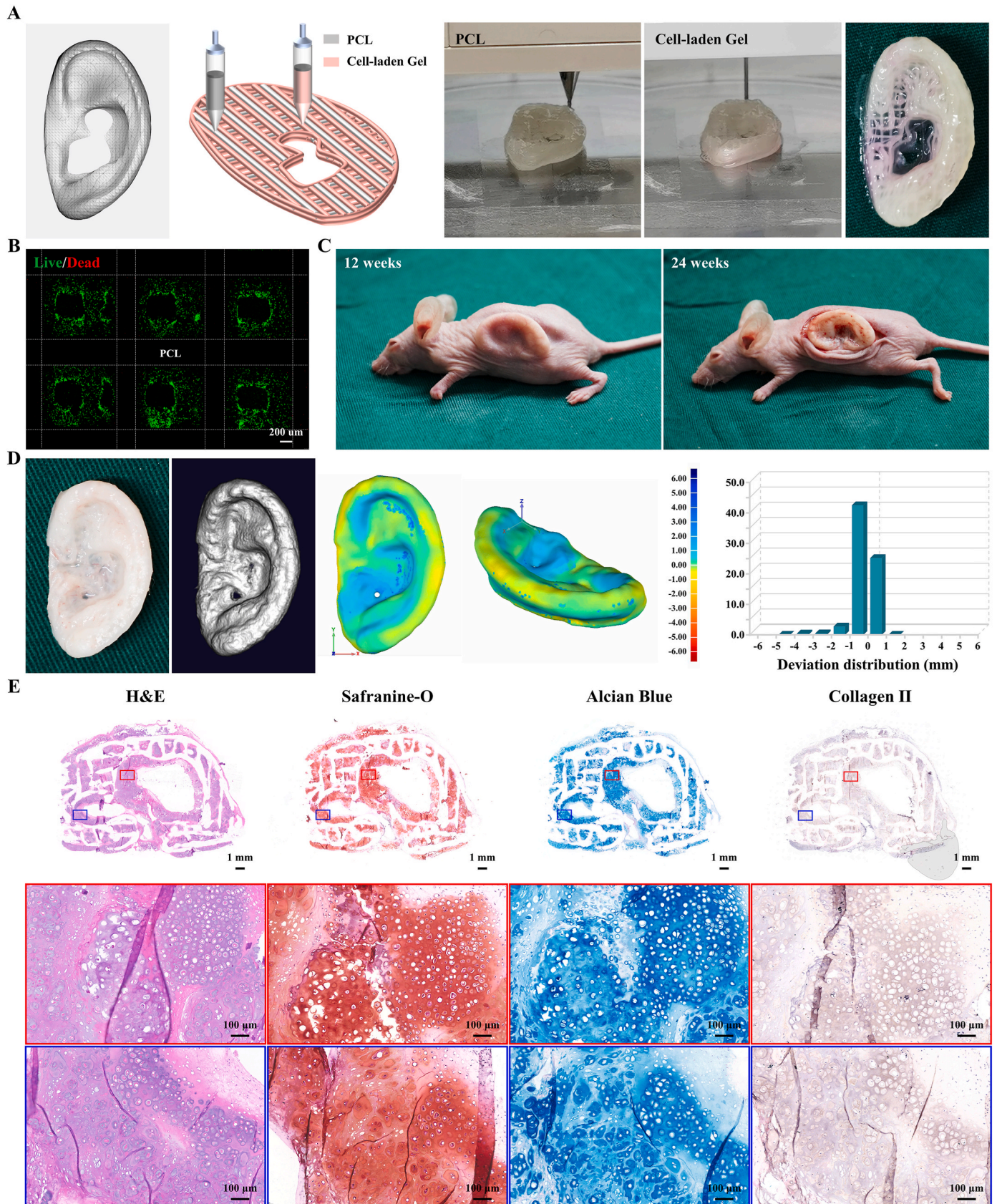
**Fig. 7.** Bioprinting and regeneration of auricular cartilage using ACMMA-based microporous bioink with PCL support. A) The 3D digital model of human auricle and bioprinting auricular equivalents based on ACMMA-based microporous bioink and PCL. B) Live/Dead staining of bioprinted auricular constructs. C) Regenerating auricular cartilage after 12 and 24 weeks of culture in nude mice. D) 3D reconstruction and 3D deviation comparison of regenerated auricular cartilage. E) H&E, Safranin-O, Alcian blue, and Collagen II staining of regenerated auricular cartilage after 24 weeks of culture *in vivo*. (For interpretation of the references to color in this figure legend, the reader is referred to the Web version of this article.)
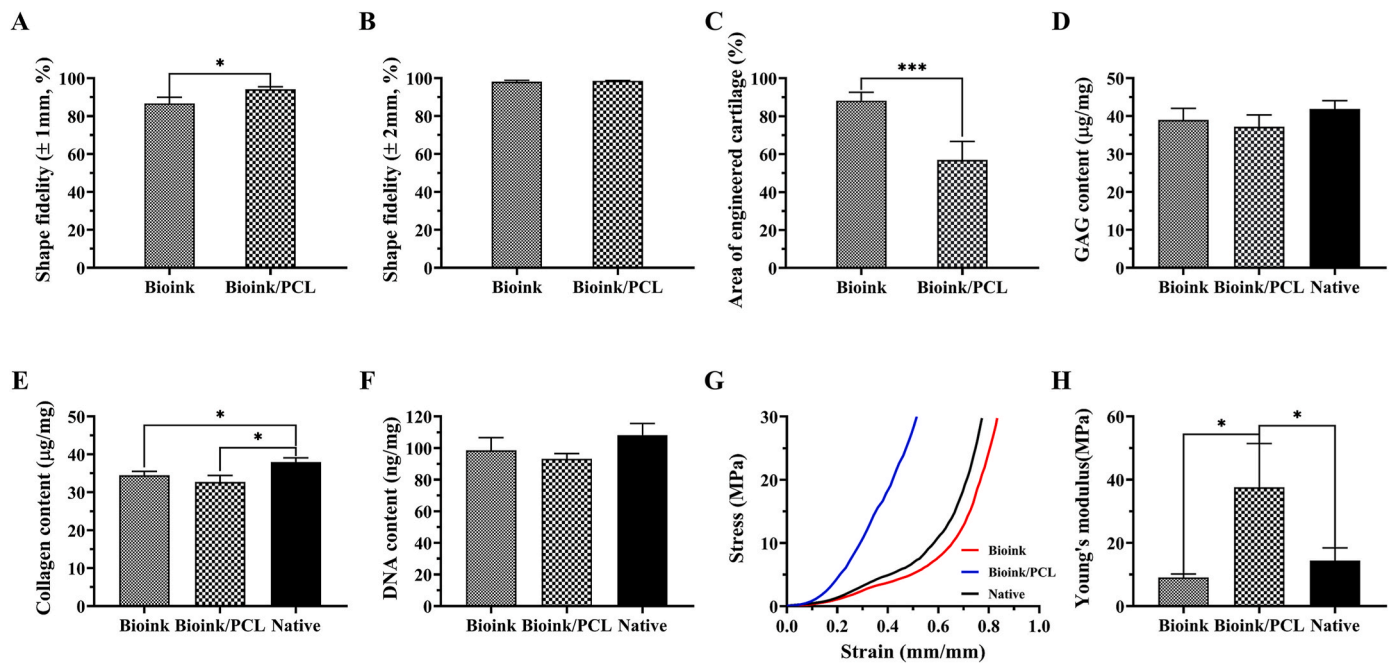
**Fig. 8.** Quantitative analysis of regenerated auricular cartilage. Shape fidelity of regenerated auricular cartilage within the deviation of A) ± 1 mm and B) ± 2 mm. C) Quantification of the area of engineered cartilage. Biochemical and biomechanical evaluation of D) GAG content, E) collagen content, F) DNA content, G) stress–strain curves, and H) Young's modulus of regenerated auricular cartilage. $*p < 0.05$. $***p < 0.001$.

### Declaration of competing interest

The authors declare that they have no known competing financial interests or personal relationships that could have appeared to influence the work reported in this paper.

### Acknowledgments

### Appendix B. Supplementary data

Supplementary data to this article can be found online at https://doi.org/10.1016/j.bioactmat.2022.02.032.

### References

[1] D.V. Luquetti, C.L. Heike, A.V. Hing, M.L. Cunningham, T.C. Cox Microtia, Epidemiology and genetics, Am. J. Med. Genet. 158A (1) (2012) 124–139, https://doi.org/10.1002/ajmg.a.34352.

[2] R.A. Bly, A.D. Bhrany, C.S. Murakami, K.C. Sie, Microtia reconstruction, Facial Plast Surg Clin North Am 24 (4) (2016) 577–591, https://doi.org/10.1016/j.fsc.2016.06.011.

[3] L. Paput, A.E. Czeizel, F. Banhidy, Possible multifactorial etiology of isolated microtia/anotia–a population-based study, Int. J. Pediatr. Otorhinolaryngol. 76 (3) (2012) 374–378, https://doi.org/10.1016/j.ijporl.2011.12.012.

[4] D. Li, W. Chin, J. Wu, Q. Zhang, F. Xu, Z. Xu, R. Zhang, Psychosocial outcomes among microtia patients of different ages and genders before ear reconstruction, Aesthetic Plast. Surg. 34 (5) (2010) 570–576, https://doi.org/10.1007/s00266-010-9502-1.

[5] B. Brent, Microtia repair with rib cartilage grafts: a review of personal experience with 1000 cases, Clin. Plast. Surg. 29 (2) (2002) 257–271, https://doi.org/10.1016/s0094-1298(01)00013-x, vii.

[6] Q. Zhang, R. Zhang, F. Xu, P. Jin, Y. Cao, Auricular reconstruction for microtia: personal 6-year experience based on 350 microtia ear reconstructions in China, Plast. Reconstr. Surg. 123 (3) (2009) 849–858, https://doi.org/10.1097/PRS.0b013e318199f057.

[7] R. Magritz, R. Siegert, Auricular reconstruction: surgical innovations, training methods, and an attempt for a look forward, Facial Plast. Surg. 30 (2) (2014) 183–193, https://doi.org/10.1055/s-0034-1371907.

[8] E.M. Ronde, M. Esposito, Y. Lin, F.S. van Etten-Jamaludin, N.W. Bulstrode, C.C. Breugem, Long-term complications of microtia reconstruction: a systematic review, J. Plast. Reconstr. Aesthetic Surg. 74 (12) (2021) 3235–3250, https://doi.org/10.1016/j.bjps.2021.08.001.

[9] Z. Yin, D. Li, Y. Liu, S. Feng, L. Yao, X. Liang, C. Miao, Y. Xu, M. Hou, R. Zhang, W. Zhang, W. Liu, Y. Liu, G. Zhou, Y. Cao, Regeneration of elastic cartilage with accurate human-ear shape based on PCL strengthened biodegradable scaffold and expanded microtia chondrocytes, Appl Mater Today 20 (2020), https://doi.org/10.1016/j.apmt.2020.100724.

[10] Y. Cao, J.P. Vacanti, K.T. Paige, J. Upton, C.A. Vacanti, Transplantation of chondrocytes utilizing a polymer-cell construct to produce tissue-engineered cartilage in the shape of a human ear, Plast. Reconstr. Surg. 100 (2) (1997) 297–302, https://doi.org/10.1097/00006534-199708000-00001, discussion 303-294.

[11] J.P. Vacanti, R. Langer, Tissue engineering: the design and fabrication of living replacement devices for surgical reconstruction and transplantation, Lancet 354 (Suppl 1) (1999) SI32–34, https://doi.org/10.1016/s0140-6736(99)90247-7.

[12] G. Zhou, H. Jiang, Z. Yin, Y. Liu, Q. Zhang, C. Zhang, B. Pan, J. Zhou, X. Zhou, H. Sun, D. Li, A. He, Z. Zhang, W. Zhang, W. Liu, Y. Cao, In vitro regeneration of patient-specific ear-shaped cartilage and its first clinical application for auricular reconstruction, EBioMedicine 28 (2018) 287–302, https://doi.org/10.1016/j.ebiom.2018.01.011.

[13] Y. Liu, D. Li, Z. Yin, X. Luo, W. Liu, W. Zhang, Z. Zhang, Y. Cao, Y. Liu, G. Zhou, Prolonged in vitro precultivation alleviates post-implantation inflammation and promotes stable subcutaneous cartilage formation in a goat model, Biomed. Mater. 12 (1) (2016), 015006, https://doi.org/10.1088/1748-605X/12/1/015006.

[14] L. Jia, Y. Zhang, L. Yao, P. Zhang, Z. Ci, W. Zhang, C. Miao, X. Liang, A. He, Y. Liu, S. Tang, R. Zhang, X. Wang, Y. Cao, G. Zhou, Regeneration of human-ear-shaped cartilage with acellular cartilage matrix-based biomimetic scaffolds, Appl Mater Today 20 (2020), https://doi.org/10.1016/j.apmt.2020.100639.

[15] Y. Gao, K. Peng, S. Mitragotri, Covalently crosslinked hydrogels via step-growth reactions: crosslinking chemistries, polymers, and clinical impact, Adv. Mater. 33 (25) (2021), e2006362, https://doi.org/10.1002/adma.202006362.

[16] D. Chimene, R. Kaunas, A.K. Gaharwar, Hydrogel bioink reinforcement for additive manufacturing: a focused review of emerging strategies, Adv. Mater. 32 (1) (2020), e1902026, https://doi.org/10.1002/adma.201902026.

[17] E. Zeimaran, S. Pourshahrestani, A. Fathi, N. Razak, N.A. Kadri, A. Sheikhi, F. Baino, Advances in bioactive glass-containing injectable hydrogel biomaterials for tissue regeneration, Acta Biomater. 136 (2021) 1–36, https://doi.org/10.1016/j.actbio.2021.09.034.

[18] A.M. Jorgensen, J.J. Yoo, A. Atala, Solid organ bioprinting: strategies to achieve organ function, Chem. Rev. 120 (19) (2020) 11093–11127, https://doi.org/10.1021/acs.chemrev.0c00145.

[19] Z. Jin, Y. Li, K. Yu, L. Liu, J. Fu, X. Yao, A. Zhang, Y. He, 3D printing of physical organ models: recent developments and challenges, Adv. Sci. 8 (17) (2021), e2101394, https://doi.org/10.1002/advs.202101394.

[20] C. Mota, S. Camarero-Espinosa, M.B. Baker, P. Wieringa, L. Moroni Bioprinting, From tissue and organ development to in vitro models, Chem. Rev. 120 (19) (2020) 10547–10607, https://doi.org/10.1021/acs.chemrev.9b00789.

[21] A.C. Daly, M.E. Prendergast, A.J. Hughes, J.A. Burdick, Bioprinting for the biologist, Cell 184 (1) (2021) 18–32, https://doi.org/10.1016/j.cell.2020.12.002.

[22] P. Fisch, N. Broguiere, S. Finkielsztein, T. Linder, M. Zenobi-Wong, Bioprinting of cartilaginous auricular constructs utilizing an enzymatically crosslinkable bioink, Adv. Funct. Mater. 31 (16) (2021), https://doi.org/10.1002/adfm.202008261.

[23] Y. Chen, J. Zhang, X. Liu, S. Wang, J. Tao, Y. Huang, W. Wu, Y. Li, K. Zhou, X. Wei, S. Chen, X. Li, X. Xu, L. Cardon, Z. Qian, M. Gou, Noninvasive in vivo 3D bioprinting, Sci. Adv. 6 (23) (2020), eaba7406, https://doi.org/10.1126/sciadv.aba7406.

[24] H.W. Kang, S.J. Lee, I.K. Ko, C. Kengla, J.J. Yoo, A. Atala, A 3D bioprinting system to produce human-scale tissue constructs with structural integrity, Nat. Biotechnol. 34 (3) (2016) 312–319, https://doi.org/10.1038/nbt.3413.

[25] N. Bhamare, K. Tardalkar, P. Parulekar, A. Khadilkar, M. Joshi, 3D printing of human ear pinna using cartilage specific ink, Biomed. Mater. 16 (5) (2021), https://doi.org/10.1088/1748-605X/ac15b0.

[26] B.S. Kim, S. Das, J. Jang, D.W. Cho, Decellularized extracellular matrix-based bioinks for engineering tissue- and organ-specific microenvironments, Chem. Rev. 120 (19) (2020) 10608–10661, https://doi.org/10.1021/acs.chemrev.9b00808.

[27] F. Pati, J. Jang, D.H. Ha, S. Won Kim, J.W. Rhie, J.H. Shim, D.H. Kim, D.W. Cho, Printing three-dimensional tissue analogues with decellularized extracellular matrix bioink, Nat. Commun. 5 (2014) 3935, https://doi.org/10.1038/ncomms4935.

[28] D.O. Visscher, H. Lee, P.P.M. van Zuijlen, M.N. Helder, A. Atala, J.J. Yoo, S.J. Lee, A photo-crosslinkable cartilage-derived extracellular matrix bioink for auricular cartilage tissue engineering, Acta Biomater. 121 (2021) 193–203, https://doi.org/10.1016/j.actbio.2020.11.029.

[29] K. Yue, G. Trujillo-de Santiago, M.M. Alvarez, A. Tamayol, N. Annabi, A. Khademhosseini, Synthesis, properties, and biomedical applications of gelatin methacryloyl (GelMA) hydrogels, Biomaterials 73 (2015) 254–271, https://doi.org/10.1016/j.biomaterials.2015.08.045.

[30] K. Yu, X. Zhang, Y. Sun, Q. Gao, J. Fu, X. Cai, Y. He, Printability during projection-based 3D printing, Bioact Mater 11 (2022) 254–267, https://doi.org/10.1016/j.bioactmat.2021.09.021.

[31] G.L. Ying, N. Jiang, S. Maharjan, Y.X. Yin, R.R. Chai, X. Cao, J.Z. Yang, A.K. Miri, S. Hassan, Y.S. Zhang, Aqueous two-phase emulsion bioink-enabled 3D bioprinting of porous hydrogels, Adv. Mater. 30 (50) (2018), e1805460, https://doi.org/10.1002/adma.201805460.

[32] G. Ying, N. Jiang, C. Parra, G. Tang, J. Zhang, H. Wang, S. Chen, N.P. Huang, J. Xie, Y.S. Zhang, Bioprinted injectable hierarchically porous gelatin methacryloyl hydrogel constructs with shape-memory properties, Adv. Funct. Mater. 30 (46) (2020), https://doi.org/10.1002/adfm.202003740.

[33] Z. Jian, T. Zhuang, T. Qinyu, P. Liqing, L. Kun, L. Xujiang, W. Diaodiao, Y. Zhen, J. Shuangpeng, S. Xiang, H. Jingxiang, L. Shuyun, H. Libo, T. Peifu, Y. Qi, G. Quanyi, 3D bioprinting of a biomimetic meniscal scaffold for application in tissue engineering, Bioact Mater 6 (6) (2021) 1711–1726, https://doi.org/10.1016/j.bioactmat.2020.11.027.

[34] P.D. Dalton, T.B.F. Woodfield, V. Mironov, J. Groll, Advances in hybrid fabrication toward hierarchical tissue constructs, Adv. Sci. 7 (11) (2020) 1902953, https://doi.org/10.1002/advs.201902953.

[35] P.M. Crapo, T.W. Gilbert, S.F. Badylak, An overview of tissue and whole organ decellularization processes, Biomaterials 32 (12) (2011) 3233–3243, https://doi.org/10.1016/j.biomaterials.2011.01.057.

[36] M.L. Hennrich, N. Romanov, P. Horn, S. Jaeger, V. Eckstein, V. Steeples, F. Ye, X. Ding, L. Poisa-Beiro, M.C. Lai, B. Lang, J. Boultwood, T. Luft, J.B. Zaugg, A. Pellagatti, P. Bork, P. Aloy, A.C. Gavin, A.D. Ho, Cell-specific proteome analyses of human bone marrow reveal molecular features of age-dependent functional decline, Nat. Commun. 9 (1) (2018) 4004, https://doi.org/10.1038/s41467-018-06353-4.

[37] P. Qiu, M. Li, K. Chen, B. Fang, P. Chen, Z. Tang, X. Lin, S. Fan, Periosteal matrix-derived hydrogel promotes bone repair through an early immune regulation coupled with enhanced angio- and osteogenesis, Biomaterials 227 (2020) 119552, https://doi.org/10.1016/j.biomaterials.2019.119552.

[38] X. Wu, M. Zhou, F. Jiang, S. Yin, S. Lin, G. Yang, Y. Lu, W. Zhang, X. Jiang, Marginal sealing around integral bilayer scaffolds for repairing osteochondral defects based on photocurable silk hydrogels, Bioact Mater 6 (11) (2021) 3976–3986, https://doi.org/10.1016/j.bioactmat.2021.04.005.

[39] J. Chen, J. Yang, L. Wang, X. Zhang, B.C. Heng, D.A. Wang, Z. Ge, Modified hyaluronic acid hydrogels with chemical groups that facilitate adhesion to host

[40] M. Hirsch, A. Charlet, E. Amstad, 3D printing of strong and tough double network granular hydrogels, Adv. Funct. Mater. 31 (5) (2020), https://doi.org/10.1002/adfm.202005929.

[41] Y. Hua, H. Xia, L. Jia, J. Zhao, D. Zhao, X. Yan, Y. Zhang, S. Tang, G. Zhou, L. Zhu, Q. Lin, Ultrafast, tough, and adhesive hydrogel based on hybrid photocrosslinking for articular cartilage repair in water-filled arthroscopy, Sci. Adv. 7 (35) (2021), https://doi.org/10.1126/sciadv.abg0628.

[42] M. Hou, B. Tian, B. Bai, Z. Ci, Y. Liu, Y. Zhang, G. Zhou, Y. Cao, Dominant role of in situ native cartilage niche for determining the cartilage type regenerated by BMSCs, Bioact Mater (2021), https://doi.org/10.1016/j.bioactmat.2021.11.007.

[43] Y. Xu, J. Zhou, C. Liu, S. Zhang, F. Gao, W. Guo, X. Sun, C. Zhang, H. Li, Z. Rao, S. Qiu, Q. Zhu, X. Liu, X. Guo, Z. Shao, Y. Bai, X. Zhang, D. Quan, Understanding the role of tissue-specific decellularized spinal cord matrix hydrogel for neural stem/progenitor cell microenvironment reconstruction and spinal cord injury, Biomaterials 268 (2021) 120596, https://doi.org/10.1016/j.biomaterials.2020.120596.

[44] T. Shen, K. Dai, Y. Yu, J. Wang, C. Liu, Sulfated chitosan rescues dysfunctional macrophages and accelerates wound healing in diabetic mice, Acta Biomater. 117 (2020) 192–203, https://doi.org/10.1016/j.actbio.2020.09.035.

[45] Y. Liu, L. Zhang, G. Zhou, Q. Li, W. Liu, Z. Yu, X. Luo, T. Jiang, W. Zhang, Y. Cao, In vitro engineering of human ear-shaped cartilage assisted with CAD/CAM technology, Biomaterials 31 (8) (2010) 2176–2183, https://doi.org/10.1016/j.biomaterials.2009.11.080.

[46] E.T. Pashuck, M. Stevens, From clinical imaging to implantation of 3D printed tissues, Nat. Biotechnol. 34 (3) (2016) 295–296, https://doi.org/10.1038/nbt.3503.

[47] A. Schwab, R. Levato, M. D'Este, S. Piluso, D. Eglin, J. Malda, Printability and shape fidelity of bioinks in 3D bioprinting, Chem. Rev. 120 (19) (2020) 11028–11055, https://doi.org/10.1021/acs.chemrev.0c00084.

[48] S. Van Belleghem, L. Torres Jr., M. Santoro, B. Mahadik, A. Wolfand, P. Kofinas, J. P. Fisher, Hybrid 3D printing of synthetic and cell-laden bioinks for shape retaining soft tissue grafts, Adv. Funct. Mater. 30 (3) (2020), https://doi.org/10.1002/adfm.201907145.

[49] H. Kim, B. Kang, X. Cui, S.H. Lee, K. Lee, D.W. Cho, W. Hwang, T.B.F. Woodfield, K. S. Lim, J. Jang, Light-activated decellularized extracellular matrix-based bioinks for volumetric tissue analogs at the centimeter scale, Adv. Funct. Mater. 31 (32) (2021), https://doi.org/10.1002/adfm.202011252.

[50] T. Aubert, J.Y. Huang, K. Ma, T. Hanrath, U. Wiesner, Porous cage-derived nanomaterial inks for direct and internal three-dimensional printing, Nat. Commun. 11 (1) (2020) 4695, https://doi.org/10.1038/s41467-020-18495-5.

[51] H.P. Lee, L. Gu, D.J. Mooney, M.E. Levenston, O. Chaudhuri, Mechanical confinement regulates cartilage matrix formation by chondrocytes, Nat. Mater. 16 (12) (2017) 1243–1251, https://doi.org/10.1038/nmat4993.

[52] Y. Yang, Q. Zhang, T. Xu, H. Zhang, M. Zhang, L. Lu, Y. Hao, J.H. Fuh, X. Zhao, Photocrosslinkable nanocomposite ink for printing strong, biodegradable and bioactive bone graft, Biomaterials 263 (2020) 120378, https://doi.org/10.1016/j.biomaterials.2020.120378.

[53] G. Cidonio, M. Glinka, J.I. Dawson, R.O.C. Oreffo, The cell in the ink: improving biofabrication by printing stem cells for skeletal regenerative medicine, Biomaterials 209 (2019) 10–24, https://doi.org/10.1016/j.biomaterials.2019.04.009.

[54] L.N. West-Livingston, J. Park, S.J. Lee, A. Atala, J.J. Yoo, The role of the microenvironment in controlling the fate of bioprinted stem cells, Chem. Rev. 120 (19) (2020) 11056–11092, https://doi.org/10.1021/acs.chemrev.0c00126.

[55] W. Sun, B. Starly, A.C. Daly, J.A. Burdick, J. Groll, G. Skeldon, W. Shu, Y. Sakai, M. Shinohara, M. Nishikawa, J. Jang, D.W. Cho, M. Nie, S. Takeuchi, S. Ostrovidov, A. Khademhosseini, R.D. Kamm, V. Mironov, L. Moroni, I.T. Ozbolat, The bioprinting roadmap, Biofabrication 12 (2) (2020), 022002, https://doi.org/10.1088/1758-5090/ab5158.

[56] B. Kong, Y. Chen, R. Liu, X. Liu, C. Liu, Z. Shao, L. Xiong, X. Liu, W. Sun, S. Mi, Fiber reinforced GelMA hydrogel to induce the regeneration of corneal stroma, Nat. Commun. 11 (1) (2020) 1435, https://doi.org/10.1038/s41467-020-14887-9.

[57] H. Sun, H. Mei, C. Song, X. Cui, P. Wang, The in vivo degradation, absorption and excretion of PCL-based implant, Biomaterials 27 (9) (2006) 1735–1740, https://doi.org/10.1016/j.biomaterials.2005.09.019.

[58] F.E. Freeman, P. Pitacco, L.H.A. van Dommelen, J. Nulty, D.C. Browe, J.Y. Shin, E. Alsberg, D.J. Kelly, 3D bioprinting spatiotemporally defined patterns of growth factors to tightly control tissue regeneration, Sci. Adv. 6 (33) (2020), eabb5093, https://doi.org/10.1126/sciadv.abb5093.

tissues enhance cartilage regeneration, Bioact Mater 6 (6) (2021) 1689–1698, https://doi.org/10.1016/j.bioactmat.2020.11.020.